Three-Dimensional Flowfield in a Turbine Nozzle Passage

M. Zaccaria,* D. Ristic,† and B. Lakshminarayana‡
Pennsylvania State University, University Park, Pennsylvania 16802

Detailed measurements were taken in the nozzle of a low-speed, single-stage, axial-flow turbine at two axial planes inside the nozzle and on the nozzle and endwall surfaces. Velocity, turbulence, and angle measurements were taken at midchord with a laser doppler velocimeter, whereas a five-hole probe was used to measure the pressure, velocities, and angles just upstream of the trailing edge. Nozzle surface and endwall static pressures were also measured. These measurements were compared to measurements previously completed at two axial planes downstream of the nozzle. The results show that, at midchord, the secondary flow seems to be weak and it is in the early stages of development. Just upstream of the trailing edge, the secondary flow is clearly visible. The radially inward flow near the suction surface augments the casing passage vortex, while counteracting the hub passage vortex. Traveling downstream, the casing passage vortex remains strong, while at the hub, the radially inward flow of the suction surface boundary layer has reversed direction because of the rotating hub. The passage-averaged velocities compare well with Katsanis and McNally's quasi-three-dimensional code and a Navier–Stokes code. These and other data are presented, interpreted, and synthesized to understand the nozzle flowfield.

Nomenclature

C = nozzle axial chord
C_p = nozzle static pressure coefficient, $(p - P_{01})/0.5\rho V_{x1}^2$
H = spanwise distance, $(R - R_h)/(R_t - R_h)$
P = stagnation pressure
PS = pressure surface
p = static pressure on nozzle surface
R = radius
Re = Reynolds number
S = percentage pitchwise distance from nozzle pressure surface to nozzle suction surface
SS = suction surface
Tu = turbulence intensity, $[\sqrt{(v_x'^2 + v_\theta'^2)}/V] \times 100$
U_m = blade speed at midspan
V = velocity
$(V_r)_{\text{ref}}$ = radial velocity at midspan passage, midspan
v' = fluctuations in velocity
X = axial distance from nozzle leading edge
β = yaw angle, measured from axial direction
β_p = primary flow angle
ζ = total pressure loss coefficient, $(P_{01} - P_0)/0.5\rho V_{x1}^2$
η = efficiency
Θ = angular position in degrees measured from the wake center at midspan
ρ = density
ψ_s = static pressure drop coefficient, $(p_1 - p)/0.5\rho V_{x1}^2$
ω = vorticity, Eq. (2)
ω_s = streamwise vorticity, Eq. (3)

Subscripts
h, t = hub, tip
m = midspan

n = normal
ref = reference conditions
r, s = rotor, stator
r, θ, x = radial, tangential, and axial directions
sec = secondary flow
0 = total
1 = inlet to nozzle
2 = exit to nozzle

Superscripts
$^-$ = circumferentially mass-averaged properties
$^=$ = area-averaged properties
$'$ = fluctuating quantity

Introduction

THE turbine nozzle flow is three dimensional and contains numerous vortices, including the passage vortex, horseshoe vortex, trailing filament and trailing shed vortices, and a corner vortex. The interaction of all these vortices causes the flow in the nozzle passage to be very complex and three dimensional. Many researchers have conducted experiments to try to understand the nozzle flowfield. Based on these experiments, a description of the flowfield in a linear turbine cascade has been derived.[1-3] A short summary is given next.

The incoming boundary layer at both endwalls separates at the leading edge of the nozzle, forming a horseshoe vortex with two counter-rotating legs: 1) the pressure side leg and 2) the suction side leg. As the pressure side leg enters the vane passage, it is convected toward the suction surface of the vane, because of the pressure gradient between the pressure and suction surfaces. It meets the suction surface near the minimum static pressure point. As the pressure side leg moves across the passage, it merges with the passage vortex, while entraining low-energy boundary-layer fluid from the endwall and blade surfaces. The suction leg of the horseshoe vortex follows the contour of the blade suction surface, until it reaches the point where the pressure side leg meets the suction side. At this point it leaves the endwall and circles around the outer edge of the passage vortex as it moves downstream. It is hard to detect this downstream of the vane, since it loses intensity because of its interaction with the passage vortex.

While this is a good description of the flow in a linear cascade, it is not an accurate one of the flow in an actual turbine nozzle. The annular design of an actual nozzle causes a radial

pressure gradient that can be on the same order of magnitude as the pitchwise pressure gradient. Also, Boletis and Sieverding[4] state that the presence of a downstream rotor causes local changes to the outlet flow of an annular cascade. Though there have been a few tests done in annular cascades, most of them have been in configurations where there is no rotor behind the nozzle,[5] or with a nozzle–rotor gap that is much larger than is found in modern axial flow turbines.[6,7] Hence, there is a need to investigate the flowfield in an annular turbine nozzle with a downstream rotor and a realistic nozzle–rotor gap (which is 20–25% of nozzle axial chord for modern turbines). This prompted the present investigation.

The overall objective of the research reported in this article is to gain a better understanding of the three-dimensional pressure and flowfield in nozzle vanes in a single-stage turbine (with a close rotor–nozzle gap), including the entire passage flow, formation and effect of horseshoe and passage vortices, and losses. An additional objective is to provide benchmark quality data for the validation of computational fluid dynamic codes. Once the nozzle flowfield is well understood, interaction of this flow with the downstream rotor, including unsteady pressure and flowfields and unsteady shear stress will be studied. Details of the nozzle exit flow, including wakes, are reported by Zaccaria and Lakshminarayana.[8]

Experimental Facility and Instrumentation

The Axial Flow Turbine Research Facility (AFTRF) of the Pennsylvania State University is an open circuit facility 91.66 cm (3 ft) in diameter and a hub-to-tip radius ratio of 0.73, with an advanced axial turbine blading configuration designed by General Electric Aircraft Engine division personnel. The facility consists of a large bellmouth inlet, a turbulence generating grid section, followed by a test section with a nozzle vane guide row and a rotor. There are 23 nozzle guide vanes and 29 rotor blades followed by outlet guide vanes. Detailed design of the facility, performance, and geometric features are described in Ref. 9. Some important performance and geometrical parameters are as follows: hub/tip ratio = 0.7269, nozzle; vane chord (tip) = 0.1768 m, vane spacing (tip) = 0.1308 m, turning angle = 70 deg, rotor; blade chord (tip) = 0.1028 m, turning angle = 95.42 deg (tip), 125.69 deg (root), tip clearance = 1.27 mm, speed = 1300 rpm; and Re of nozzle flow (based on exit flow) = 10^6, mass flow rate = 11.05 kg/s, pitchline loading coefficient = 1.9, design η_s = 0.9421, η_r = 0.8815. The nozzle–rotor gap is 22.5% of nozzle axial chord at midspan.

A schematic of the facility and nozzle vane profile is given in Ref. 8. The variation of the vane shape is small from tip to midspan of the vane, whereas it is larger from midspan to the hub. Measurement locations are shown in Fig. 1. The inlet freestream turbulence intensity varies from 1 to 2%. Measurements were taken at five different axial locations in the AFTRF nozzle from one chord upstream of the nozzle to X_m/C_m = 1.09. Measurements at X_m/C_m = −1.0, 1.025, and 1.09 were reported previously.[8] Measurements inside the passage (X_m/C_m = 0.56 and 0.935) are reported and interpreted in this article. A window for LDV measurements covering the entire flowfield from upstream of the nozzle to downstream of the rotor passage is incorporated. The data processing system is completely automated.

The nozzle vane has one fully instrumented passage with 154 static pressure taps at several chordwise and radial locations on the suction and pressure surfaces and on the casing and hub walls. The static pressure holes on the vane surfaces are more closely spaced near the hub and the tip since the vane surface static pressure distribution changes more rapidly in this region because of the complexity of the endwall flow.

Laser Doppler Velocimeter (LDV) System

The LDV is a Thermo Systems, Inc. (TSI) two-color, four-beam, two-dimensional measuring system. It consists of a 7-W argon–ion laser tuned to the 488 nm (blue) and 514.5
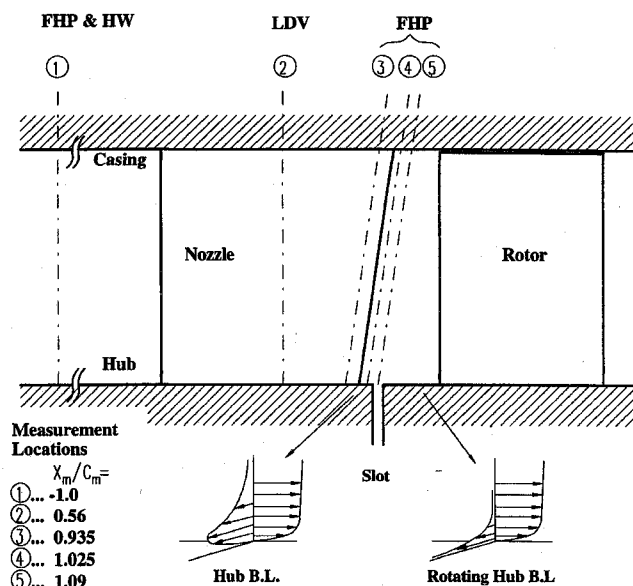

Fig. 1 Nozzle flowfield measurement locations.

(green) lines. These beams are then split and one beam of each color is passed through a Bragg cell where it is frequency shifted. The half-angle of the beams is 4.95 deg and the length of the probe volume is 0.65 mm. Atomized mineral oil was used as seeding in the nozzle. TSI's six-jet seeder is used to atomize the oil. A 25.4-mm-(1-in.-) diam tube is connected to the atomizer and is positioned 0.9 m (3 ft) upstream of the AFTRF bellmouth intake [1.5 m (5 ft) upstream of the nozzle]. The seeding tube can be moved radially and circumferentially to optimize the data rate each time the LDV probe volume is moved. Scattered light from the atomized oil particles passing through the probe volume is collected on-axis.

The LDV system is mounted on an optical table that is attached to a mechanical traverse. The traverse can move vertically, parallel, and perpendicular to the AFTRF axis (the axial and radial directions, respectively), and also can be tilted. The three linear degrees of freedom plus tilt enables very accurate positioning of the probe volume. The flow in the AFTRF is measured through a curved Plexiglas® window, conforming to the inside of the casing. The Plexiglas is 4.76 mm (3/16 in.) thick. The nozzle, rotor, and endwalls were painted with a high-temperature flat black paint to reduce surface reflections. Regular flat black paint was first used, but the laser beams burned off the paint. To process the data, two countertype signal processors (one for each channel) are interfaced with an IBM PC compatible computer. The two components are taken in coincidence with a coincidence window typically of 50 μs.

LDV Measurement Errors

The error in locating the probe volume is ±0.5 mm, which is ±0.8% of blade span at midpitch. Errors in the measurement arise because of fluctuations in the flowfield and random noise in the photomultiplier tube signal, statistical or velocity bias, and angle bias. The error in the mean flow velocity measurement, for a confidence level of 95%, was estimated to be about 0.2% using the standard small sample method.[10] The error caused by velocity gradient is assumed to be negligible because any spatial variation of the flowfield in a region as small as the probe volume is very small. Statistical or velocity bias is introduced to a small extent by the temporal variation of the velocity magnitude, while data rate variations contribute most of the bias. Data rate variations occur since in flows with uniform seeding, more particles traverse the probe volume per unit time when the velocity is higher than the mean velocity than when the velocity is lower than the mean velocity. Thus a high data rate causes the measured values to be biased to-

ward a higher value than the true mean. An estimate of the error caused by statistical bias is found to be less than 0.5% and is described in more detail by Zaccaria.[10] Angle bias occurs when the flow is not parallel to the plane containing the laser beams. The factor controlling the angle bias is the ratio N/N_{fr}, where N is the minimum number of cycles required by the signal processor and N_{fr} is the number of measurable fringes. The angle bias can be minimized by reducing the N/N_{fr} ratio. Frequency shifting was used to minimize the angle bias and therefore this error is negligible.

Five-Hole Probe

A five-hole probe was used to measure the flowfield inside of the nozzle. The five-hole probe is a miniature one, with a probe head diameter of 1.67 mm. The five-hole probe was calibrated so that it could measure flows with a velocity direction oriented ±30 deg to the probe tip in both the yaw and pitch directions. The estimated errors in the five-hole probe measurements are given by Sitaram et al.,[11] and are as follows: wall and blade vicinity effects, Reynolds and Mach number effects, misalignment of probe, probe blockage effect, and turbulence effects. The wall vicinity effect error is less than 1%, two or more probe diameters away from the wall. To account for measurements within two probe diameters of the wall, the probe was calibrated for the wall vicinity effects similar to Ref. 11.

The probe was calibrated over the same range of Reynolds numbers that occur in the measurement locations, thus the Reynolds number effects have been accounted for. The probe is aligned to an accuracy of ±0.25 deg. Since the probe is calibrated to an accuracy of ±0.50 deg, the error in the yaw and pitch angle is ±0.75 deg. The error in the axial position is ±0.40 mm, the error in the radial position is ±0.01 mm, and the error in the tangential position is ±0.04 deg. The error in the probe blockage is negligible, since the probe was calibrated with its supporting structure and the ratio of the probe diameter to both the vane spacing and pitch is 1.4 and 1.5%, respectively. The pressure and velocity gradient error is estimated to be less than 1.0%. The error in velocity caused by turbulence effects is estimated to be 0.33% based on a turbulence intensity of 10%.

Vane Surface and Endwall Static Pressure Distribution

Contour plots of the casing and hub wall static pressure coefficients based on inlet dynamic head are shown in Figs. 2a and 2b, respectively. One unusual feature of this flowfield is that the minimum static pressure location on both the endwalls occur at the suction surface. Other researchers,[12,13] have found that minimum static pressure occurs in the passage between the two nozzle vanes. Langston et al.[12] associates this minimum static pressure with the formation of a separation region. At the casing the separation bubble seems to start, in the present case, at $X/C = 0.50$ and is consistent with the vane static pressure distribution (Fig. 3). The static pressures are very low in the corner regions formed by both the hub wall and the annulus wall with the suction surface. This is caused by the secondary flow.

Sjolander[14] found that the shear stress trajectories in the endwall regions were parallel to the pressure gradient. This shows that the fluid energy is so small that the inertial effects are insignificant. Moustapha et al.[13] state that the endwall pressure gradient is indicative of the direction of the endwall shear stress, and consequently, the direction of the flow. The cross-passage flow extends over most of the hub and casing walls. The minimum static pressure region on the hub ($C_p = -13$) occurs at $X/C = 0.8$ (downstream of the throat), whereas the minimum pressure region on the casing ($C_p = -9.5$) occurs at $X/C = 0.5$ (upstream of the throat). (The throat is located at $X/C = 0.71$ along the suction surface for the hub and at $X/C = 0.68$ on the suction surface for the casing.) Graziani et al.[15]

show that this low-pressure region is the location where the passage vortex lifts off the endwall surface and begins to grow rapidly.

Contour plots of static pressure on the nozzle pressure and suction surfaces are presented in Figs. 3a and 3b, respectively. The flowfield is two dimensional over the whole pressure surface, which is demonstrated by the relatively constant pressure coefficient values in the spanwise direction. The static pressure varies slightly from the leading edge to midchord. The pressure decreases rapidly downstream of midchord.

The nozzle suction surface flowfield is two dimensional from the leading edge to $X/C = 0.40$, with the flow accelerating rapidly from the leading edge to this point. Downstream of $X/C = 0.40$, the flowfield is three dimensional. There are two distinct three-dimensional areas downstream of $X/C = 0.40$, one at the hub and the other at the casing. The three-dimensional region near the hub wall begins at $X/C = 0.80$. As shown in Fig. 2b, the cross-passage pressure gradient drives the flow and the passage vortex toward the suction surface. The passage vortex meets the suction surface at $X/C = 0.80$ where the low pressure region occurs ($C_p = -13$) and then travels up the suction surface and toward the trailing edge. The path of the hub wall passage vortex (HPV) along the suction surface is shown in Fig. 3b. The position of the passage vortex at the trailing edge was determined from the flowfield measurements in the trailing-edge region discussed later in this article.

The three-dimensional flow on the suction surface near the casing wall begins at $X/C = 0.5$. The flow behavior is similar
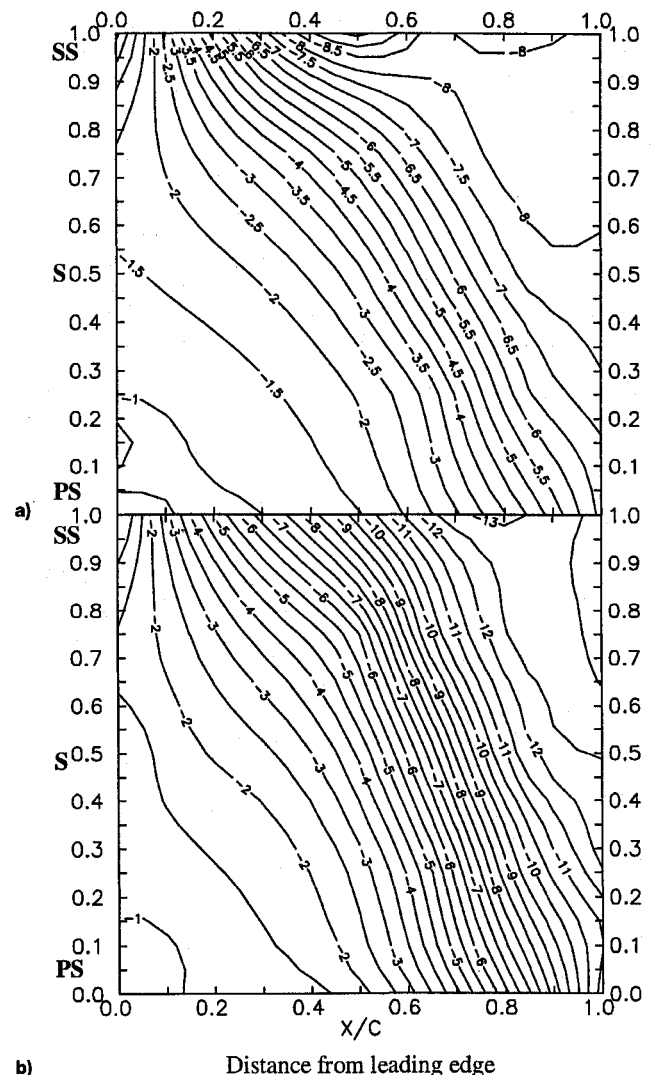
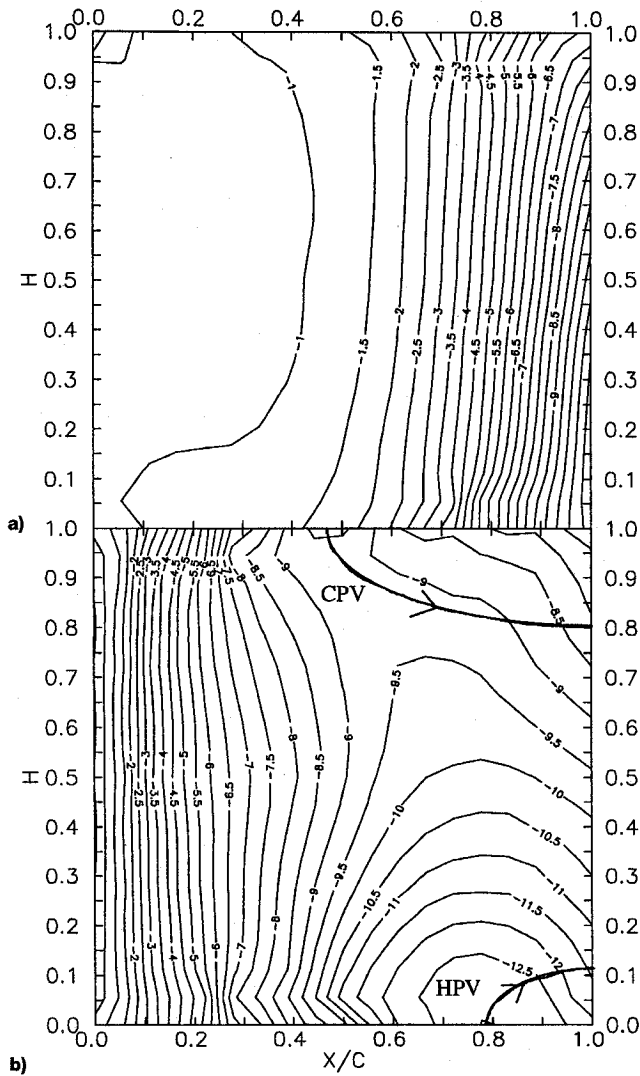Fig. 2 Contours of C_p on nozzle: a) casing and b) hub.

Fig. 3 Contours of C_p on nozzle: a) pressure and b) suction surfaces.

data could not be taken because of limited access in the nozzle. A comparison of total velocity derived from the LDV, five-hole probe and the vane surface velocity (derived from vane static pressure) at midspan is presented in Ref. 10. Both the LDV and five-hole probe data match the velocity profile quite well. This excellent comparison between various types of measurements indicates that error in the five-hole probe and LDV data is negligibly small.

to that of the hub wall region with the casing passage vortex traveling toward the suction surface as shown in Fig. 2a. The passage vortex meets the suction surface at the low pressure point ($C_p = -9.5$), which occurs at $X/C = 0.50$, and then the casing passage vortex (CPV) sweeps down the suction surface toward the trailing edge, following the path shown in Fig. 3b. The position of the passage vortex at the trailing edge was determined from the flowfield measurements in the trailing-edge region. One interesting feature of this flowfield, is that contrary to what occurs in a linear cascade, the casing passage vortex intersects the suction surface farther upstream ($X/C = 0.50$) than the hub passage vortex intersects the suction surface ($X/C = 0.80$).

Nozzle Passage Flowfield

Flowfield near Midchord ($X_m/C_m = 0.56$)

Two-component LDV measurements were taken at one axial plane inside the nozzle from hub-to-tip and from blade-to-blade. Since the nozzle axial chord decreases from hub-to-tip and the LDV measurement plane is at a constant axial distance downstream of the leading edge of the nozzle, the measuring location as a percent chord decreases from hub-to-tip ($X/C = 0.61$ at $H = 0.05$ and $X/C = 0.52$ at $H = 0.95$). $X_m/C_m = 0.56$ will be used to define this axial plane.

The LDV measurements at $X_m/C_m = 0.56$ are shown in Fig. 4. The blank areas in the contour plots represent regions where
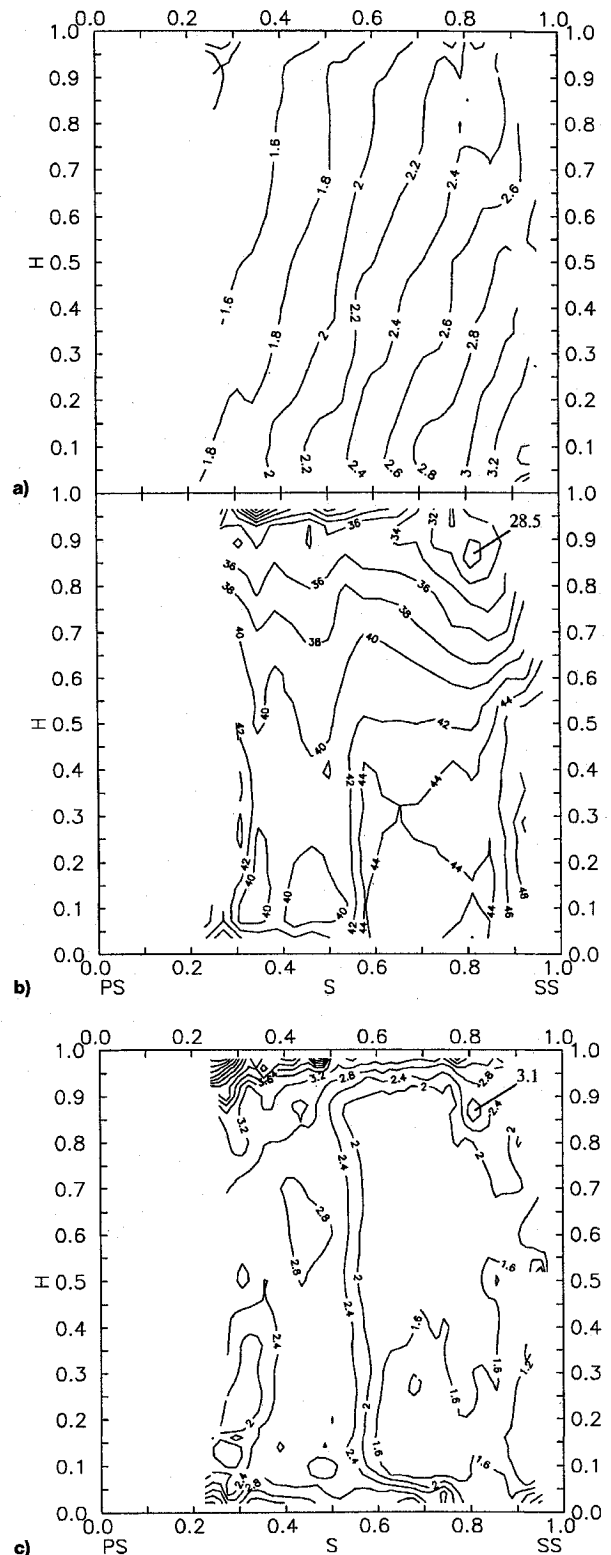

Fig. 4 LDV measurements at $X_m/C_m = 0.56$: a) V/V_{x1}, b) β in degrees, and c) Tu at $X_m/C_m = 0.56$.

Total velocity contours are presented in Fig. 4a. The tangential distance is normalized by the distance between the pressure and suction sides where $S = 0$ is the pressure surface and $S = 1$ is the suction surface. The total velocity variation follows the usual inviscid trend. The yaw angle contours, presented in Fig. 4b, show a rather well-behaved flow with a ± 2-deg variation across the pitch at most locations. (The design mean flow angle is 40 deg at this axial location.) As expected in inviscid flow, the turning angle near the suction surface is higher than that near the pressure surface. There is a region of high underturning in the corner formed by the casing and suction side. The angle at that location is 28.5 deg. This could be because of the passage secondary flow. The overturning region associated with this vortex could not be observed because of the constraints imposed by the LDV measurement limitations. The secondary flow seems to be rather weak and it is in the early stages of development. This is also confirmed by the turbulence intensity contours (Fig. 4c) that show that the maximum turbulence intensity in this region is about threefold compared to 1% at the inlet. Increased levels of turbulence intensity occur in the passage vortex.[16] No evidence of secondary flow is seen at the hub. In addition to the secondary flow phenomenon, one can observe the development of the annulus wall boundary layer, which is thin (less than 5% of span). The increased turbulence intensity both in the hub region and in the tip regions is evident in Fig. 4c.

Flowfield near the Trailing Edge ($X_m/C_m = 0.935$)

Near the trailing edge, the flowfield was surveyed with a five-hole probe. A five-hole probe was employed to facilitate stagnation pressure loss evaluation as well as to measure the blade endwall flows more thoroughly. The axial plane position ranges from $X/C = 0.93$ at the hub to 0.94 at the tip. The axial plane position will be defined by the axial distance at midspan, $X_m/C_m = 0.935$. Data were taken at 23 spanwise locations, clustered near the endwalls, and 40–55 tangential locations clustered near the vane surfaces.

Stagnation and Static Pressures

Figure 5a shows the stagnation pressure loss coefficient ζ. The two high-loss regions located in the corner formed by the suction surface and the annulus wall as well as the suction surface and the hub wall show that the secondary flow is fairly well developed here. These high-loss regions are associated with the passage vortex caused by the secondary flow. High losses occur in the core region and the maximum loss coefficient observed is 4.7 near the tip and 6.0 near the hub. The tip loss core is located farther from the casing than the hub loss core is from the hub. This is a result of the radial inward velocities that exist in both the freestream and the vane boundary layer. The radial inward flow and the wake transport increases the loss coefficient near the hub region to a greater extent than those observed in the tip region. This is consistent with the measurements made slightly downstream of the trailing edge[8] at $X_m/C_m = 1.025$. A comparison of the losses in the two axial planes show that the loss contours are very similar in the tip and the hub regions, indicating no major redistribution of the losses as the flow progresses from $X_m/C_m = 0.935$–1.025.

Another noticeable feature of this flowfield is that the casing passage vortex covers more area than the hub passage vortex. This results from three reasons. The first is the radial inward velocities result in inward movement of the hub passage vortex towards the hub, which causes it to be compressed, while the casing passage vortex moves away from the casing. The second reason can be found in the discussion of the nozzle endwall and surface static pressure contours presented earlier (Figs. 2 and 3). These static pressure contours show that the casing passage vortex formation occurs farther upstream than the hub passage vortex does. Since the passage vortex begins to grow rapidly after it intersects with the suction surface, the casing passage vortex has a larger area because of the longer
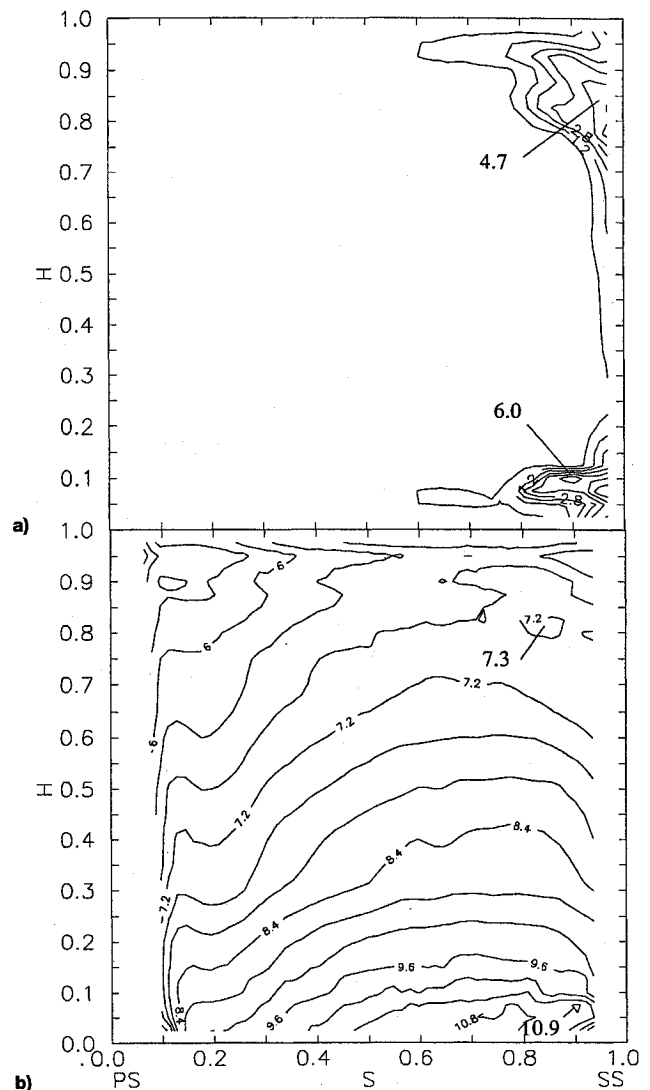

Fig. 5 Five-hole probe measurements at $X_m/C_m = 0.935$: a) ζ coefficient and b) ψ_s coefficient.

distance it has traveled between the endwall/suction surface intersection point and this measuring location. The third reason is that the casing inlet boundary layer is thicker than the hub wall boundary layer, which also results in the larger extent of the casing passage vortex.

The contours of ψ_s at this location are given in Fig. 5b. At most locations the behavior is as expected in an inviscid flow, except in the corner formed by the annulus wall and the suction surface where there is a low-pressure region (static pressure coefficient is 7.3), indicating the presence of secondary flow and possibly a vortex. A similar patch can be seen near the hub surface as well.

Velocity and Flow Angles

Figure 6a shows the total velocity contours. The total velocity increases from the tip to the hub because of the existence of the radial pressure gradient discussed earlier. A low-velocity region is observed near the corner formed by the suction surface and hub and casing walls. This is the region of intense mixing of secondary flow and wall and blade boundary layers.

One of the more interesting features of this flowfield is the yaw angle shown in Fig. 6b. Most of the flow turning has taken place at this location and the maximum overturning of about 8 deg occurs at $H = 0.85$ close to the suction side. The maximum underturning region (about 4 deg) is observed slightly below ($H = 0.80$) and a little farther from the suction side than

Fig. 6 Measurements at $X_m/C_m = 0.935$: a) V/V_{x1} and b) β in degrees.

at $X_m/C_m = 0.935$ was taken from the measured flow angle at the midspan at the respective tangential position, since the flow at midspan was not affected by the secondary flow, whereas downstream of the nozzle the primary flow angle was set equal to the design exit angle (70.0 deg). Using this procedure, the secondary velocities were derived from

$$\underline{V}_{sec} = \underline{r}V_r + \underline{n}V_n = (\underline{V})_{measured} - (\underline{V})_{design} \qquad (1)$$

where V_r is the radial velocity and V_n is the velocity normal to the streamwise direction (estimated as previously indicated). To perceive the secondary flow more clearly, the radial velocity at midspan and at midpitch [$(V_r)_{ref}$] is subtracted from the velocity vectors. At $X_m/C_m = 0.935$ (Fig. 7a), the passage vortex (clockwise) can be clearly seen near the suction surface/ casing corner. Since the pressure side leg of the horseshoe vortex has the same direction of rotation as the passage vortex, this vortex could be a combination of the passage vortex and the pressure side leg of the horseshoe vortex. Other researchers[1,2] believe that the pressure side leg of the horseshoe vortex merges with the passage vortex and the results here do not show otherwise. There is no evidence of the suction side leg of the horseshoe vortex near the casing (which would rotate opposite to the passage vortex).

the overturning region. This over and underturning of the flow is characteristic of a vortex. Outside the secondary flow regions the yaw angle variation is only 4 deg across most of the passage. A similar secondary flow region can be observed near the hub. The maximum overturning is about 3 deg with a similar magnitude of underturning close to the suction side. This seems to indicate a conventional secondary flow pattern both in the hub and tip region. In addition, the flow very close to the walls, across the entire passage is overturned slightly, because of the hub wall boundary layer.

The magnitude of radial velocity can be discerned from the radial flow angle distribution.[10] Negative values of radial flow angle indicate that flow is toward the hub. Radial flow angles indicate that the flow is inward over most of the passage. There are two locations, near the corners formed by the suction surface with the endwalls, where maximum and minimum values can be observed relative to the surrounding regions. Near the casing the maximum radial flow angle observed is -59 deg and the minimum is 1 deg, whereas near the hub the maximum radial flow angle is -34 deg and the minimum is 6 deg. These high- and low-radial flow angles are another indication of the presence of passage vortices.

Secondary Flow Vectors

The secondary flow vectors in the $r-\theta$ plane, shown in Fig. 7, are derived from the measured data. The primary flow angle

Fig. 7 a) Secondary flow vectors [V_{sec}, Eq. (1)] at $X_m/C_m = 0.935$, $(V_r)_{ref}$ subtracted and **b)** secondary velocity vectors near the hub-suction side corner at $X_m/C_m = 0.935$, $(V_r)_{ref}$ subtracted.

Radial inward flow exists in the vane boundary layers due to imbalance between the centrifugal force and the pressure gradient inside the boundary layer. This imbalance between the centrifugal and the pressure forces generates radial inward flow, which continues even in the wake. This radial inward flow is in the same direction as those induced by the casing passage vortex close to the suction side and thus it augments the passage vortex. At the hub, on the other hand, there is evidence of a passage vortex, but it is much weaker than the vortex near the casing. The radial inward flow in the suction surface boundary layer near the hub is in the opposite direction to those caused by the passage vortex, and thus the radial inward flow seems to overshadow those induced by the passage vortex. This is shown more clearly in Fig. 7b, which is an enlargement of the secondary velocity vectors near the hub/suction side corner. The passage vortex in this figure is labeled P. Above the passage vortex, there seems to be a weak vortex rotating in the opposite direction. This could be the suction side leg of the horseshoe vortex and it is labeled H_{ss} in this figure.

The secondary velocity vectors [obtained by subtracting $(V_r)_{\text{ref}}$] at $X_m/C_m = 1.025$ are shown in Fig. 8a. In this figure Θ is in degrees and $\Theta = 0.0$ is the wake center at midspan, with the suction surface of the upstream vane to the left of the wake center and the pressure side to the right of the wake center ($\Theta = 15.65$ deg is one vane pitch). At $X_m/C_m = 1.025$, the passage vortex near the casing is well developed. At the same radius on the pressure side of the wake, there is a vortex that rotates in the opposite direction. This vortex is formed by the interaction of the passage vortex and the wake. At the hub, the passage vortex is still visible, although it is very weak. The suction side leg of the horseshoe vortex is very weak or nonexistent. The radial inward flow of the suction surface boundary layer, observed at $X_m/C_m = 1.025$, seems to have disappeared. In fact, the flow on the suction side of the wake near the hub has reversed direction and is moving radially outward. This is a result of the rotating hub that is located just downstream of this location. The rotation of the hub is toward increasing Θ in this figure. The hub wall boundary layer is highly skewed and undergoes sudden perturbation as shown in Fig. 1.

Figure 8b shows the secondary flow velocity vectors at $X_m/C_m = 1.09$. Near the casing, the passage vortex is still visible. On the other hand, the hub passage vortex is not visible. It is anticipated that the rotating hub could have caused the passage vortex to diffuse. The radial inward flow at the hub is caused by the gap between the stationary and rotating hub at this location.

Comparing Figs. 7 and 8, no dramatic change in secondary flow is observed at the tip as the flow progresses downstream. The migration of the passage vortex towards the wake center as one travels from $X_m/C_m = 0.935$ to $X_m/C_m = 1.09$ is observed, while the spanwise location of the vortex has not changed. This is in contrast to the results of Moore and Adhye,[17] where the passage vortex in their turbine rotor cascade (with larger turning than the present case) migrates toward midspan and toward the middle of the passage as it progresses downstream. The secondary flow at the hub, however, undergoes a dramatic change from $X_m/C_m = 0.935$ to $X_m/C_m = 1.09$. This is a result of the rotating hub that interacts with the secondary flow at the hub.

Streamwise Vorticity

The components of vorticity in the axial, tangential and radial directions are given by

$$\omega_x = \frac{\partial V_r}{r\partial \theta} - \frac{\partial(rV_\theta)}{r\partial r}, \quad \omega_\theta = \frac{\partial V_x}{\partial r} - \frac{\partial V_r}{\partial x}, \quad \omega_r = \frac{\partial V_\theta}{\partial x} - \frac{1}{r}\frac{\partial V_x}{\partial \theta}$$
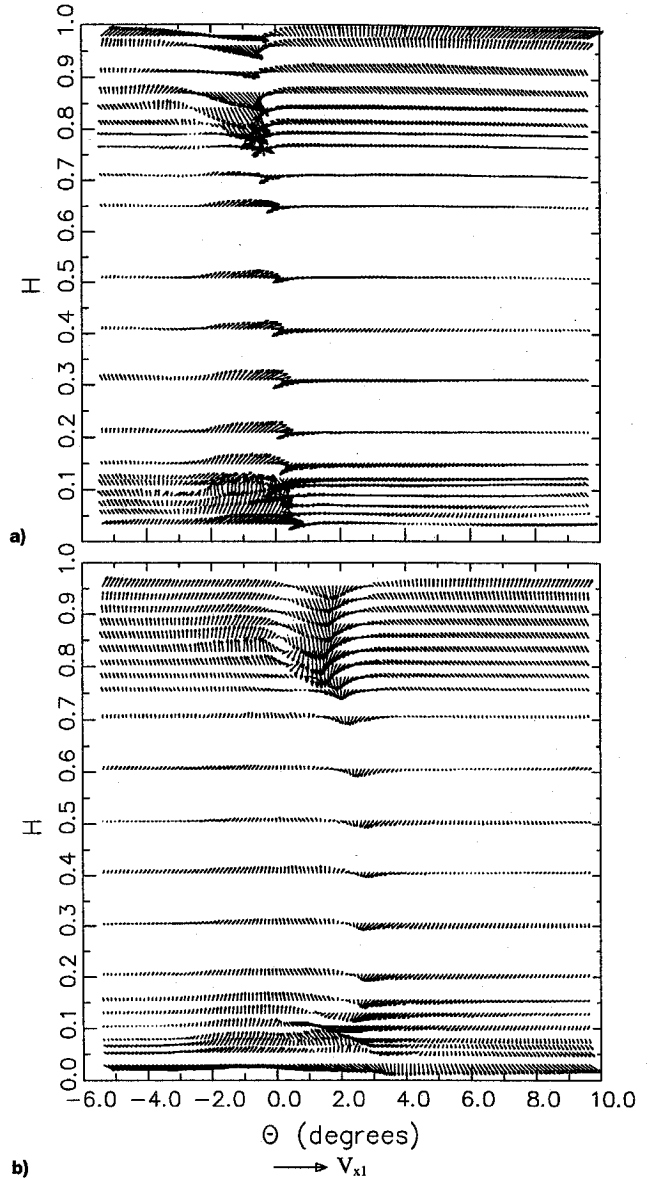
(2)

a)

b)

————➤ V_{x1}

Fig. 8 Secondary velocity vectors $(V_r)_{\text{ref}}$ subtracted. $X_m/C_m =$ a) 1.025 and b) 1.09.

The streamwise vorticity is then given by

$$\omega_s = \omega_x \cos \beta_p + \omega_\theta \sin \beta_p + \omega_r \sin \alpha$$

(3)

where α is the radial flow angle. The streamwise vorticity is normalized by C/V_{x1}. The primary flow angle is determined as previously indicated. The streamwise vorticity derived from the data at $X_m/C_m = 0.935$ is shown in Fig. 9. The secondary vorticity at $X_m/C_m = 1.025$ and 1.09 are given in Ref. 8. At $X_m/C_m = 1.025$, the vorticity was found explicitly using the data measured at the axial plane $X_m/C_m = 1.09$ to determine the axial gradients. But at $X_m/C_m = 0.935$, measurements were not made at an axial plane inside the vane close enough to this location to determine the axial gradients, and so another method had to be used to estimate the axial gradients. Gregory-Smith et al.[18] have developed a method to estimate the axial gradients, based on the inviscid equation $\rho \underline{V} \times \underline{\omega} = \nabla P_0$. The components of vorticity are given by

$$\omega_r = \frac{1}{V_x}\left(\frac{1}{\rho r}\frac{\partial p}{\partial \theta} + \frac{1}{2r}\frac{\partial V^2}{\partial \theta} + V_r \omega_x\right)$$

$$\omega_\theta = -\frac{1}{V_x}\left(\frac{1}{\rho}\frac{\partial p}{\partial r} + \frac{1}{2}\frac{\partial V^2}{\partial r} + V_\theta \omega_x\right)$$

(4)

Thus, with the radial and tangential vorticity now known, the streamwise vorticity can be derived. The streamwise vorticity is normalized with respect to inlet axial velocity and vane chord at midspan.

The passage vortex near the casing at $X_m/C_m = 0.935$ is shown clearly in Fig. 9. The large positive vorticity (magnitude of 30.0) in the suction surface/casing corner corresponds to the passage vortex. Near the hub wall/suction surface corner, a large negative vorticity region (magnitude of -14.1) is caused by the hub passage vortex. The large positive vorticity region above the passage vortex could possibly correspond to the suction side leg of the horseshoe vortex. The vorticity is zero in the freestream giving confidence in this method used to calculate vorticity. At $X_m/C_m = 1.025$ (shown in Ref. 8), the peak magnitude of vorticity near the casing has decreased by about half. This is because of the interaction of the passage vortex and the wake. The large negative vorticity region near the casing (magnitude of -11.3) is because of the vortex rotating in the opposite direction that is caused by the interaction of the passage vortex and the wake flow (compare Figs. 7a and 8a). On the other hand, the negative vorticity region near the hub has not changed very much in strength between the two locations.

Five criteria are used to determine the existence of a vortex in a flowfield. These are high total pressure loss, low static pressure, high vorticity, over and underturning of the yaw angle, and positive and negative radial flow angles. A vortex exists when these five features occur at the same position in the flowfield. The existence of the passage vortices at both the

hub and the casing of $X_m/C_m = 0.935$ is confirmed since they both meet all five of the criteria. On the other hand, the existence of the suction side leg of the horseshoe vortex is more doubtful. There is no evidence of its existence in the casing/suction side corner. While in the hub/suction side corner there is a region of high positive vorticity that could correspond to the suction side leg of the horseshoe vortex, the other criteria are not met. Thus, its existence cannot be proven conclusively.

Mass-Averaged Properties

The circumferentially mass-averaged total pressure loss profiles at various locations from upstream of the nozzle to downstream of the nozzle are shown in Fig. 10 (the properties upstream of the nozzle inlet for all of the following figures are a single radial traverse). The stagnation pressure loss profile at the nozzle inlet shows the boundary-layer thickness to be approximately 10% at the hub and 15% at the tip. At $X_m/C_m = 0.935$, 1.025, and 1.09, the upstream boundary-layer profile losses have been subtracted, hence, those represent the losses occurring within the nozzle passage. At all three axial locations, there are two loss peaks. The peak near the hub is larger in magnitude but smaller in radial extent than the one near the casing. The larger inlet casing boundary layer results in the larger extent of the secondary flow region near the casing. The larger magnitude of the hub loss region is a result of the radial inward flow of the boundary layer and wake, which cause the low momentum fluid in the boundary layer and wake to move toward the hub.

Many additional features can also be seen from this figure. The profile losses nearly double between $X_m/C_m = 0.935-1.025$. This is caused by separation near the trailing-edge region and the mixing of this flow with the boundary-layer flow. The profile losses are nearly constant along the span ($H = 0.2-0.8$), except in the endwall region. The measured peak secondary loss near the casing region decreases 10–20% from $X_m/C_m = 0.935-1.09$, and the peak loss location moves inward as the flow progresses downstream. On the other hand, the hub secondary losses (both the magnitude and the profile) are nearly constant from $X_m/C_m = 0.935-1.025$.

The measured mass-averaged total pressure loss profiles in Fig. 10 are compared to mass-averaged total pressure loss profiles computed using a Navier–Stokes code.[19] This code uses a four-stage Runge–Kutta scheme and an algebraic Reynolds stress model is employed for turbulence closure. The total pressure profiles predicted using the Navier–Stokes code compare well with the experimental data upstream of the nozzle trailing edge, whereas the agreement between the computational and experimental data is not very good downstream of the trailing edge. At $X_m/C_m = 0.935$ the computation agrees well with the experimental data near the tip, whereas at the hub, the location of the loss peak is predicted correctly, but the magnitude is not. Downstream of the trailing edge, the
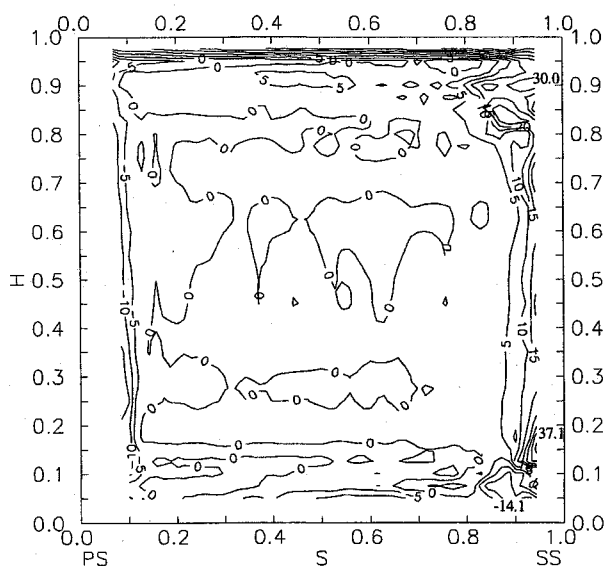
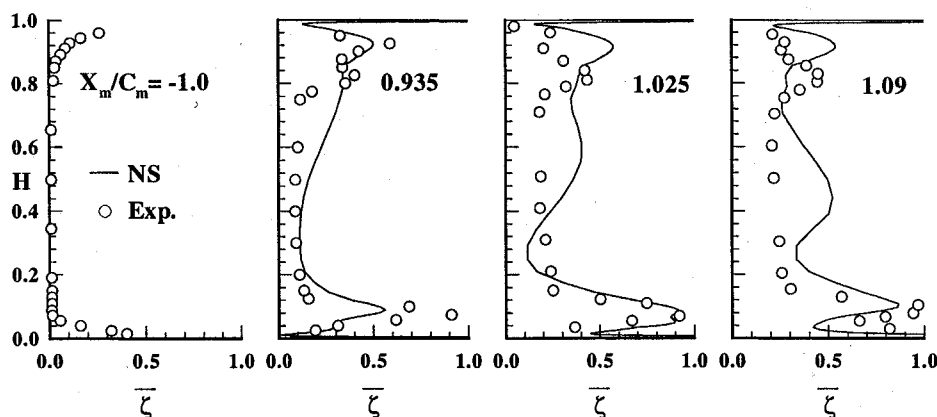Fig. 9   Streamwise vorticity $(\omega_s C_m/V_{x1})$, at $X_m/C_m = 0.935$.

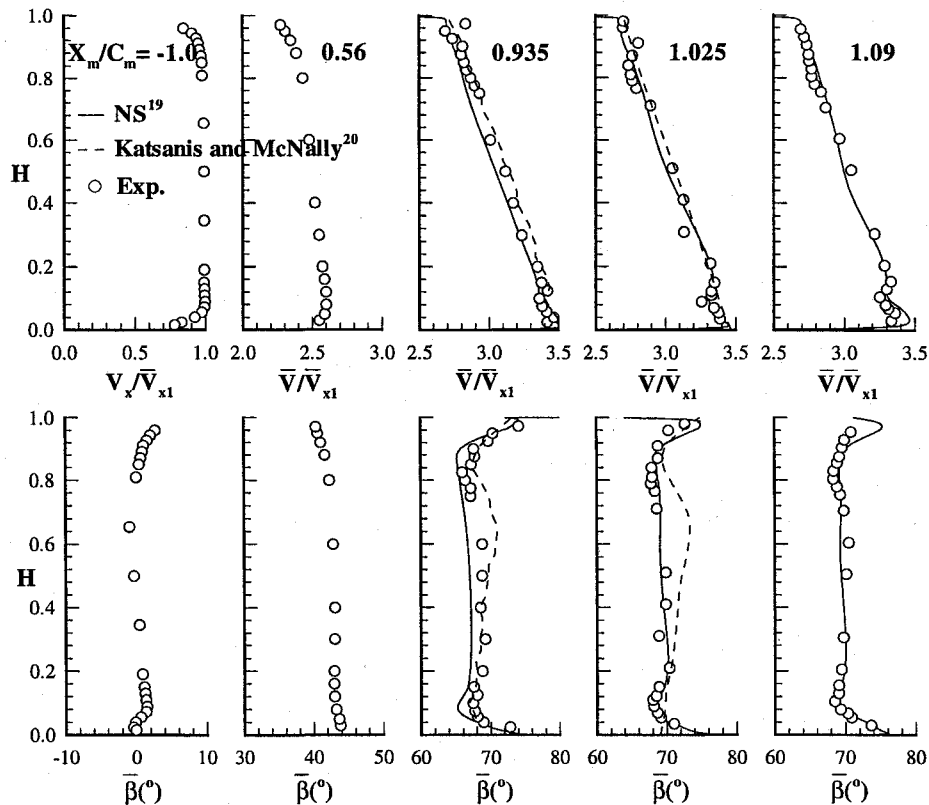Fig. 10   Radial distribution of pitch- (mass-) averaged $\bar{\zeta}$.

Fig. 11   Radial distribution of pitch- (mass-) averaged $\overline{V}/\overline{V}_{x1}$ and β in degrees.
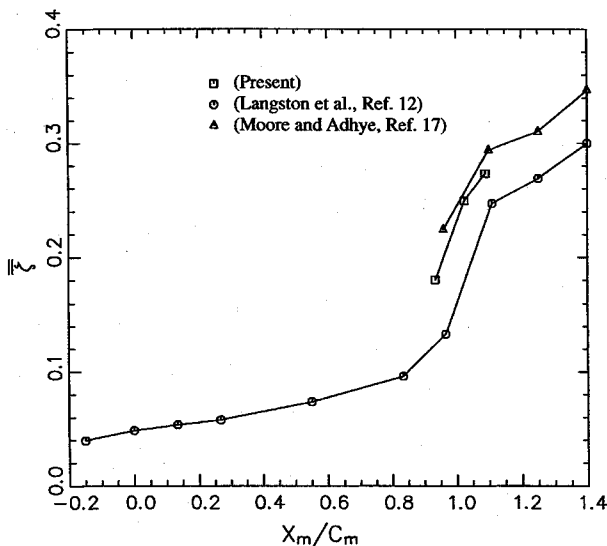

Fig. 12   Axial variation of area and $\bar{\zeta}$.

measured loss agrees well with the prediction, but near the tip, the location of the loss peak is incorrect.

The mass-averaged total velocity is shown in Fig. 11. The boundary-layer profile is clearly visible upstream of the nozzle inlet. At $X_m/C_m = 0.935-1.09$, the total velocity profiles show a sharp decrease in velocity near $H = 0.10$ and a more gradual decrease in velocity near $H = 0.80$, which is because of the hub and tip wall secondary flow, respectively. The total velocity predicted using the quasi-three-dimensional code of Katsanis and McNally[20] and the Navier–Stokes code are compared with the total velocity measured at $X_m/C_m = 0.935$ and 1.025. The agreement is excellent between the experimental data and both computations.

The mass-averaged yaw angle is also shown in Fig. 11. The yaw is derived from the mass-averaged tangential velocity and

the mass-averaged axial velocity. At the nozzle inlet ($X_m/C_m = -1.0$), the yaw angle is about zero everywhere. The yaw angles at $X_m/C_m = 0.56$ show the presence of weak secondary flow. From $X_m/C_m = 0.935-1.09$, the yaw angle shows overturning at the casing and hub endwalls. As one moves away from the endwalls, the flow becomes underturned, achieving design flow from $H = 0.1-0.8$. This is consistent with the predictions from secondary flow theories and measurements by others. The largest overturning is about 5 deg, and this is much smaller than those reported by others for rotor cascades. The yaw angle at $X_m/C_m = 0.935$ and 1.025 is compared to both Katsanis and McNally's[20] inviscid code and Luo and Lakshminarayana's[19] Navier–Stokes code predictions. The agreement is excellent between the Navier–Stokes code predictions and the experimental data, whereas the inviscid code's agreement is only fair near the endwalls and accurate to within ±2 deg everywhere else. The inviscid code's prediction even captures the overturning at the casing. This demonstrates the usefulness of using an inviscid code in turbomachinery design.

Figure 12 shows the area-averaged stagnation pressure loss coefficient and is compared with two other turbine cascades. The AFTRF nozzle follows the same trend as the other turbine blades, increasing as one moves downstream. The large increase in losses going from $X_m/C_m = 0.935-1.025$ is partly caused from the separation that occurs at the vane's trailing edge and partly from the fact that the vane surface boundary layer could not be completely measured close to the wall (thus giving a lower area-averaged loss), whereas downstream of the nozzle the losses in the entire wake could be measured. The loss growth downstream of the nozzle trailing edge is caused by the mixing of the flow downstream of the vane and by turbulence mixing.

Conclusions

A complete flowfield survey was carried out at two axial locations inside the nozzle passage at $X_m/C_m = 0.56$ and 0.935 and these data were compared to previously acquired data downstream of the nozzle. The nozzle surface and endwall

static pressures were also measured. The results show that at midchord, the secondary flow is weak and is in its early stages of development. Just upstream of the trailing edge (X_m/C_m = 0.935), the casing passage vortex is clearly visible in the casing/suction surface corner and is very strong. Radially inward flow in the suction surface boundary layer augments the casing passage vortex. The suction side leg of the horseshoe vortex is not visible near the casing. On the other hand, the passage vortex in the hub/suction surface corner is very weak. The radially inward flow in the suction surface boundary layer is in the opposite direction as those induced by the passage vortex and thus counteracts it. A vortex rotating in the opposite direction as the hub passage vortex is visible above the passage vortex. This might be the suction side leg of the horseshoe vortex.

The casing passage vortex remains strong as it progresses downstream and no dramatic change in secondary flow occurs at the tip. At the hub, however, the radially inward flow of the suction surface boundary layer has reversed direction and is moving outward as a result of the rotating hub.

The agreement between the Navier–Stokes code predictions and the experimental data is excellent for both the total velocity and yaw angle and reasonable for the total pressure loss coefficient. The agreement of the yaw angle and total velocity prediction by Katsanis and MacNally's code[20] and the experimental data is good, demonstrating the usefulness of using an inviscid code in early turbomachinery design.

Acknowledgments

References

[1]Langston, L. S., "Crossflows in a Turbine Cascade Passage," *Journal of Engineering for Power*, Vol. 102, No. 1, 1980, pp. 21–28.

[2]Sieverding, C. H., "Recent Progress in the Understanding of Basic Aspects of Secondary Flows in Turbine Blade Passages," *Journal of Engineering for Gas Turbines and Power*, Vol. 107, April 1985, pp. 437–444.

[3]Sharma, O. P., and Butler, T. L., "Prediction of Endwall Losses and Secondary Flows in Axial Flow Turbine Cascades," *Journal of Turbomachinery*, Vol. 109, April 1987, pp. 229–236.

[4]Boletis, E., and Sieverding, C. H., "Experimental Study of the Flow Field Behind an Annular Turbine Nozzle Guide Vane with and Without Downstream Rotor," American Society of Mechanical Engineers Paper 84-GT-15, June 1984.

[5]Sieverding, C. H., Van Hove, W., and Boletis, E., "Experimental Study of the Three-Dimensional Flow Field in an Annular Turbine Nozzle Guidevane," *Journal for Gas Turbines and Power*, Vol. 106, April 1984, pp. 437–444.

[6]Richards, P. H., and Johnson, C. G., "Development of Secondary Flows in the Stator of a Model Turbine," *Experiments in Fluids*, June 1988.

[7]Joslyn, D., and Dring, R., "Three-Dimensional Flow in an Axial Turbine," American Society of Mechanical Engineers Paper 90-GT-56, June 1990.

[8]Zaccaria, M., and Lakshminarayana, B., "Investigation of Three-Dimensional Flowfield at the Exit of a Turbine Nozzle," *Journal of Propulsion and Power*, Vol. 11, No. 1, 1995, pp. 55–63.

[9]Lakshminarayana, B., Camci, C., Halliwell, I., and Zaccaria, M., "Investigation of Three Dimensional Flow Field in a Turbine Including Rotor/Stator Interaction, Part 1: Design, Development and Performance of Turbine Facility," AIAA Paper 92-3325, July 1992.

[10]Zaccaria, M., "An Experimental Investigation of Steady and Unsteady Flow Field in an Axial Flow Turbine," Ph.D. Dissertation, Pennsylvania State Univ., University Park, PA, Dec. 1994.

[11]Sitaram, N., Lakshminarayana, B., and Ravindranath, A., "Conventional Probes for the Relative Flow Measurement in a Rotor Blade Passage," *Journal of Engineering for Power*, Vol. 102, April 1981, pp. 405–414.

[12]Langston, L. S., Nice, M. L., and Hooper, R. M., "Three-Dimensional Flow Within a Turbine Cascade Passage," *Journal of Engineering for Power*, Vol. 99, Jan. 1977, pp. 21–28.

[13]Moustapha, S. H., Paron, G. J., and Wade, J. H. T., "Secondary Flow in Cascades of Highly Loaded Turbine Blades," American Society of Mechanical Engineers Paper 85-GT-135, June 1985.

[14]Sjolander, S. A., "The Endwall Boundary Layer in an Annular Cascade of Turbine Nozzle Guide Vanes," Carlton Univ., TRME/A 75-4, Ottawa, ON, Canada, 1975.

[15]Graziani, R. A., Blair, M. F., Taylor, J. R., and Mayle, R. E., "An Experimental Study of Endwall and Airfoil Surface Heat Transfer in a Large Scale Turbine Blade Cascade," *Journal of Engineering for Power*, Vol. 102, April 1980, pp. 257–267.

[16]Gregory-Smith, D. G., and Cleak, J. G. E., "Secondary Flow Measurements in a Turbine Cascade with High Inlet Turbulence," American Society of Mechanical Engineers Paper 90-GT-20, June 1990.

[17]Moore, J., and Adhye, R., "Secondary Flows and Losses Downstream of a Turbine Cascade," *Journal of Engineering for Gas Turbines and Power*, Vol. 109, 1985, pp. 961–969.

[18]Gregory-Smith, D. G., Graves, C. P., and Walsh, J. A., "Growth of Secondary Losses and Vorticity in an Axial Turbine Cascade," *Journal of Turbomachinery*, Vol. 110, Jan. 1988, pp. 1–8.

[19]Luo, J., and Lakshminarayana, B., "Three-Dimensional Navier Stokes Computation of Turbine Nozzle Flow with Advanced Turbulence Models," American Society of Mechanical Engineers 95-GT-302, June 1995.

[20]Katsanis, T., and McNally, W., "Revised Fortran Program for Calculating Velocities and Streamlines on the Hub-Shroud Midchannel Stream Surface of an Axial-, Radial-, or Mixed Flow Turbomachine or Annular Duct. I—User's Manual," NASA TN D-8430, 1977.